Microstructure and corrosion behavior of 316L stainless steel prepared using different additive manufacturing methods

Revilla, Reynier I.; Van Calster, Matthieu; Raes, Marc; Arroud, Galid; Andreatta, Francesco; Pyl, Lincy; Guillaume, Patrick; De Graeve, Iris

Published in:
Corrosion Science

DOI:
10.1016/j.corsci.2020.108914

Publication date:
2020

Microstructure and corrosion behavior of 316L stainless steel prepared using different additive manufacturing methods: A comparative study bringing insights into the impact of microstructure on their passivity

Reynier I. Revilla [1,*], Matthieu Van Calster [1], Marc Raes[1], Galid Arroud[2], Francesco Andreatta[3], Lincy Pyl[4], Patrick Guillaume[2], Iris De Graeve [1]

[1] *Department of Materials and Chemistry, Research group of Electrochemical and Surface Engineering, Vrije Universiteit Brussel, Pleinlaan 2, 1050 Brussels, Belgium*
[2] *Department of Mechanical Engineering, AVRG, Vrije Universiteit Brussel, Pleinlaan 2, 1050 Brussels, Belgium*
[3] *Polytechnic Department of Engineering and Architecture, University of Udine, Via del Cotonificio, 108-33100 Udine, Italy*
[4] *Department of Mechanics of Materials and Constructions, Vrije Universiteit Brussel, Pleinlaan 2, 1050 Brussels, Belgium*

*Corresponding author. E-mail address: rrevilla@vub.be (R. I. Revilla)

ABSTRACT:
This work compares the microstructure and corrosion resistance of 316L stainless steel samples prepared using two different additive manufacturing methods: selective laser melting (SLM), and laser metal deposition (LMD). A wrought material was used as reference. The specimens showed marked differences in their microstructure, as a result of the specific manufacturing conditions. All samples displayed similar corrosion potential and passive current density values. However, variations were seen in their potential passive range (SLM > LMD > Wrought). The wider passivity of the SLM specimen can be associated with its finer microstructure, which leads to a more stable native oxide.

Keywords:
Additive manufacturing; 316L stainless steel; Selective laser melting; Laser metal deposition.

1. Introduction

Metal additive manufacturing (MAM), also known as metal 3D printing, is a rapidly growing industry which core business is based on the fabrication of complex metal parts with improved functionalities. During MAM, metal pieces are built-up in a layer by layer fashion using a digital 3D design [1-6]. Among the several MAM processes, those utilizing a metal powder feedstock and a laser source to achieve the metal fusion are widely used [1-6]. Two such methods are selective laser melting (SLM) and laser metal deposition (LMD). LMD is a Direct Energy Deposition technology, while SLM belongs to the Powder Bed Fusion family [7]. During SLM, the laser is used to successively melt and fuse together patterns in a metal powder bed. On the other hand, during LMD the laser beam melts the powder fed by a coaxial nozzle directly on the metallic substrate, forming a deposit that is fusion-bonded to the substrate. While the SLM method allows the fabrication of pieces with very high structural complexity at a relatively high level of precision, the dimension of the pieces is limited and the starting substrate has to be a flat surface. In contrast, the LMD process can be used on existing parts of arbitrary geometry with a relatively high deposition rate; however, the shape complexity is limited. This makes LMD a preferred methodology for repairing existing parts [8].

Besides differences in the application field and structural complexity of the final parts, SLM and LMD greatly differ in the laser parameters and powder specifications. For SLM applications, the laser power is in the range between 100 W and 300 W, while for LMD much higher values between 500 W and 1000 W are usually employed. The laser spot size is ~ 0.1 mm for SLM, however, in the case of LMD the laser spot diameter is ~ 1 mm. On the other hand, the average particle size of the powder used for SLM applications is generally smaller than the particle size used in LMD machines.

Nowadays, several alloys can be processed using MAM [1]. Amongst these alloys, 316L austenitic stainless steel is of great interest due to its numerous industrial applications. The microstructure of additively manufactured (AM) 316L stainless steel has been found to be greatly affected by the MAM processes due to the special conditions associated with these manufacturing methods (for instance, extremely high cooling rates). Numerous works have already been dedicated to the study of the microstructure of AM 316L stainless steel [8-24]. However, most of these studies were conducted on specimens prepared by SLM methods [9-19], while fewer works have been devoted to LMD 316L stainless steel specimens [8,20-24]. Nevertheless, the same type of features is found for both additive manufacturing methods. In general, AM 316L stainless steel is characterized by a very fine and interconnected network of cells (which are elongated in the direction of the thermal gradient) that are confined within larger single-crystal grains [9,10,12-18,20-22]. The diameter of these cells has been reported between 0.5 μm and 1 μm for SLM specimens [9,10,12-18], while for 316L samples prepared using the LMD method larger diameters have been reported (between 3 μm and 15 μm) [20,21,22,24]. Previous works report an enrichment of Cr [11,13,16,20-22], Mo [9-11,13,16,19-22], and even Ni [13,21] and Mn [13] at the border of these cells.

The unique microstructure of AM 316L stainless steel, seems to have a considerable impact on the corrosion behavior and passivity of these specimens. Several works have been dedicated to this topic in recent years [16-20,25-36]. Nevertheless, most of these studies have been conducted on SLM specimens. Even though a few contradictory results can be found in literature, the latest studies suggest that if no major porosities are found in SLM 316L stainless steel samples, their corrosion resistance is higher than that of specimens prepared using conventional manufacturing methods [16-18,29-35]. Some researchers concluded that the high solidification rates during SLM avoid the formation of inclusions or they are too small to play a role in pitting initiation [30,32]. Other recent reports have demonstrated that the native oxide layer of SLM 316L stainless steel has better barrier properties, than that of its wrought counterpart [34,35]. This has been associated with their special microstructure, consisting of a dense network of cells with a local chemical segregation at their borders, which could promote the growth of a dense and more stable passive oxide film [34,35]. On the contrary, the majority of the few corrosion studies conducted on 316L stainless steel samples fabricated using the LMD method have shown a lower corrosion resistance for the LMD-prepared sample compared to the wrought counterpart [20,36]. The reduced corrosion resistance in these cases has been associated with the existence of heterogeneities, small amounts of δ-ferrite, and the presence of porosity. Nevertheless, these heterogeneities and defects could possibly be due to an incorrect selection of process parameters. In a different work, Majumdar et al. [37] concluded that 316L stainless steel prepared using LMD presented a higher pitting corrosion resistance than that of the conventionally processed material.

To the best of the authors' knowledge, not only is the number of studies researching the corrosion behavior of LMD 316L stainless steel very limited, but there is also no work to date comparing the corrosion performance of 316L stainless steel materials prepared by LMD and SLM. This work compares the microstructure and corrosion resistance of LMD, SLM, and wrought 316L stainless steel. An optical and scanning electron microscopy characterization was first carried out, revealing microstructural features characteristic from each manufacturing process. After this characterization, anodic potentiodynamic polarization experiments were conducted, showing marked differences between the different samples. Even though all samples presented approximately the same corrosion potential value and passive current density, great variations were seen in their potential passive range. The possible link between the microstructural features of the samples and their passivity is discussed.

2. Materials and methods

2.1. Samples

Three 316L stainless steel samples were used in this study: a wrought specimen, and two additively manufactured samples (one prepared by laser metal deposition – LMD, and another one prepared using selective laser melting – SLM). The nominal chemical composition of 316L stainless steel is presented in Table 1. The SLM 316L specimens were prepared using a Concept Laser M2 Cusing machine in an argon atmosphere with resulting oxygen content of < 0.2 %. A

laser power of 180 W, 600 mm/s scanning speed, 25 µm layer thickness, and a spot diameter of 120 µm were used for the fabrication of the samples. The LMD 316L samples were fabricated with a Megacut machine (with in-house adaptations), using argon as shielding gas at a flow rate of 8 l/min. A laser power of 530 W, 750 mm/s scanning speed, 3.8 g/min powder mass flow rate, 5 l/min carrier gas flow rate, 0.5 mm layer thickness, and a spot diameter of 1.2 mm were used in this case. No post heat treatment was applied on the samples. All the specimens were mechanically ground and polished, finishing with 0.04 µm standard colloidal silica suspension (OP–S). The use of AM 316L in the text refers to additively manufactured 316L in a general way, which includes the LMD and SLM samples.

2.2. Electrochemical measurements

Potentiodynamic polarization experiments were carried out using an AUTOLAB Potentiostat–Galvanostat (PGSTAT 302N). A three–electrode cell configuration consisting of the sample as working electrode, a Pt counter electrode, and a saturated Ag/AgCl (210 ± 15 mV vs SHE) reference electrode was used for the experiments. The electrolyte used was a 3.5 wt.% NaCl solution at room temperature. The potentiodynamic test was conducted 75 min after immersion in the electrolyte in order to wait for the system to stabilize. The scans were performed in the anodic direction at a rate of 0.1 V/min starting 50 mV below OCP until 1.6 V above the OCP value. For each sample, at least 3 potentiodynamic polarization curves were obtained in order to confirm reproducibility of the measurements.

2.3. Sample characterization

The optical images were obtained with a Leica DMi8 optical microscope. Microstructure and corrosion morphology characterization was carried out by means of scanning electron microscopy (SEM) combined with energy dispersive X-ray spectroscopy (EDS). A FE–SEM JEOL JSM–7100F with 15 kV acceleration voltage, 5 pA probe current, and a working distance of 10 mm was used. The EDS analysis was performed with acceleration voltage between 15 kV and 20 kV, a probe current between 3 nA and 5 nA, and a working distance of 10 mm. To highlight the microstructural features, the samples were etched in Glyceregia reagent (15 ml glycerol, 15 ml HCl, and 5 ml HNO_3).

AFM topography and SKPFM measurements were conducted using a commercial atomic force microscope (Park Systems XE–100). Rectangular conductive cantilevers (ANSCM–PT from AppNano) with a Pt/Ir coating, resonant frequency of 50 – 70 kHz, and a spring constant of 1 – 5 N/m were used for the measurements. Topography and corresponding potential images were simultaneously obtained using a single-pass methodology.

3. Results

3.1. Microstructure analysis

An initial characterization of the samples was conducted using optical microscopy. Figure 1 shows optical images of the etched surface of the LMD and the SLM 316L stainless steel specimens. The laser tracks from the MAM process can be easily distinguished in these optical

images. On the surface perpendicular to the building direction (XY), overlapping elongated tracks can be seen (see Figure 1a and 1c); while on the surface parallel to the building direction (XZ) a scale-like pattern can be identified (see Figure 1b and 1d). Even though both AM samples show a similar kind of pattern, great differences can be seen in the dimension of these features. It is important to notice that the scale bar in the images of the LMD samples stands for double of the distance of that in the images of the SLM specimens. The arrows in the inset of Figures 1a and 1c are a rough representation of the average distance between the centers of two consecutive melt pools. This dimension is more than 5 times greater for the LMD sample in comparison with the SLM specimen. The much thicker melt pools found in the LMD sample compared to those in the SLM sample are the result of the typical differences in the laser characteristics between the two processes, namely, the laser spot size and laser power, as well as other parameters such as the layer thickness.

To study the samples microstructure at a lower scale, SEM combined with EDS point analysis was carried out. Figure 2 shows secondary electron micrographs at medium and high magnification for all the samples. As can be seen in Figure 2a and 2b, the wrought sample reveals typical polygonal-shape coarse grains. On the other hand, the additively manufactured samples are characterized by a dense network of cells with an etch-resistant border (see Figure 2c-f). Colonies of round and elongated cells can be easily seen on the surfaces of the AM 316L stainless steel samples. This orientation of the cells is linked with the heat gradient during solidification [12,13,22,24,31]. As mentioned in the introduction, the microstructure of AM 316L stainless steel has already been described in a great number of studies [8-24], and for both SLM and LMD 316L stainless steel, the presence of cells with an etch-resistant border has been described [8-24]. As can be seen in Figure 2c-f, these cells have an average width between 4 and 6 μm for the LMD specimen, while for the SLM sample the average width of these cells is around 0.5 μm. Therefore, the cells present in the LMD 316L specimen are on average 10 times larger than those in the SLM samples.

In this study, an EDS point analysis was conducted in the LMD specimen. Around 20 EDS spectra were acquired at the borders and the same number in the interior of multiple cells as described in the schematic of Figure 3a. This was done in etched samples as well as in freshly polished samples in order to discard any influence from the etching procedure. However, no difference was found in the results. Figure 3b shows the average and standard deviation of the elemental composition obtained from the EDS analysis. It can be clearly seen that the border of the cells is slightly enriched of Cr, Ni, Mo, Mn, and Si, while depleted in Fe in comparison with the cell's interior. The segregation of these elements at the cells borders could explain their relatively higher etching resistance. In Figure 3b can be noticed that the standard deviation of the results obtained at the cell's border is slightly larger than those obtained in the cell's interior. This is most likely due to the influence of the underlying/surrounding material (depending on the interaction volume/penetration depth of the electron beam). Nevertheless, clear shifts can be seen in the average value of the different elements' composition. Due to limitations of our equipment, EDS analysis was not possible in the very fine microstructure of the SLM material. However, the same elemental enrichment at the cell's borders has been reported in a recent work for SLM 316L stainless steel samples [13]. Moreover, Barkia et al. [21] also found an enrichment of Cr,

Ni, and Mo at the cells borders on LMD 316L specimens. Nevertheless, the researchers claim a depletion of Mn at the cell's borders, which is in contradiction with our observations.
Moreover, during the SEM analysis of the SLM and LMD samples, almost no pores (and only minor pores) were found. Therefore, the electrochemical behavior should not be affected by porosity in these samples [32]. Additionally, no inclusions could be detected in the AM 316L stainless steel specimens.

3.2. Potentiodynamic polarization measurements

Anodic polarization experiments were carried out in 3.5 wt.% NaCl. For the AM samples, experiments were conducted in the XY as well as in the XZ surface. However, as also reported in previous studies [16,31,35], no difference was found between these two planes. Therefore, only one characteristic curve was chosen per sample. Figure 4 shows the anodic polarization curves obtained for wrought, LMD, and SLM 316L stainless steel. As can be seen, the corrosion potential (E_{corr}) of all the samples is approximately the same. The average value of E_{corr} calculated taking into account the measurements conducted in all the samples was –73 ± 10 mV vs Ag/AgCl. This could be due to the fact that all the samples have approximately the same chemical composition. The similarity in E_{corr} between wrought and AM 316L stainless steel has already been reported in several previous studies for a variety of electrolytes [16,17,29-35]. Additionally, all the samples presented very similar passive current density values (Figure 4). On the other hand, great differences were observed in the passivity of the different specimens. A rather extended passive behavior can be seen for the SLM specimen in the potentiodynamic curves (see Figure 4), while the passive region of the LMD sample is situated between the SLM and the wrought material. This marked difference in the passivity breakdown of the samples was very reproducible. Table 2 presents the average value and standard deviation of the difference between the potential at which a significant increase of the anodic current is observed ($E_{breakdown}$) and E_{corr}. These values indicate the passivity range of each specimen in the anodic polarization curves. It can be seen that the passivity range of the SLM sample is two times larger than that of the LMD sample, and 2.3 times larger than the passive range of the wrought specimen. A much more extended passivity for SLM samples compared to wrought specimens has also been shown in several previous works using numerous corrosive media [16-18,29-33,35].
A closer look at the potentiodynamic polarization curves in Figure 4 also reveals noticeable differences in the slope of the current density measured after the passivity breakdown. A much steeper slope was seen after the passivity breakdown of the wrought sample compared to the AM materials. Meanwhile, the potentiodynamic curves of the LMD and SLM specimens showed a very similar slope after the passivity region. This is confirmed in the amount of charge per surface area during the anodic dissolution of the materials, calculated from the anodic polarization curves starting from the moment of passivity breakdown, shown in Figure 5. . The charge per surface area calculated for the wrought material lies between one and two orders of magnitude higher than the charge per surface area of the AM samples shortly after passivity breakdown (see Figure 5). This charge is directly proportional to the amount of material removed during the anodic dissolution of the steel substrate. Therefore, much more material is removed

after the breakdown potential during anodic polarization for the wrought sample than for the AM specimens.

3.3. Corrosion morphology

A characterization of the morphology of the corrosion attacks after potentiodynamic polarization was conducted using SEM. Figure 6 shows SEM micrographs of the corrosion attack on the surface of the wrought and the LMD 316L samples. A relatively larger superficial spreading of the corrosion was seen for the LMD samples compared to the wrought material. On the other hand, more localized and deeper attacks characterized the corrosion morphology of the wrought 316L stainless steel. In Figure 6, the SLM sample was excluded since very limited corrosion took place due to the proximity of the breakdown potential to the end potential during anodic polarization (see Figure 4). However, a very similar morphology as that of the LMD sample has been reported in previous studies for SLM [16]. Additive manufactured 316L stainless steel exhibits, in general, rather superficial corrosion morphology. Figure 7 shows higher magnification SEM images of the corrosion attack after potentiodynamic polarization for the wrought and LMD samples. A deep pit can be seen on the surface of the wrought specimen (Figure 7a), while on the surface of the LMD sample (Figures 7b and 7c) the morphology of the cells described in the previous microstructure analysis (see Figure 2) was revealed. Figures 7b and 7c show different corroded spots of the same surface (one in which the rounder side of the cells is seen and the other in which the elongated section is displayed). As can be seen in Figure 7b and 7c, the borders of these cells are highly resistant against corrosion, and only the cells' interior dissolves during anodic polarization. Figure 7b presents the round section of the cells, while Figure 7c shows the elongated side of the cells. By estimating the pitting resistance equivalent number (PREN = 1×%Cr + 3.3×%Mo + 16×%N) for the interior and the border of the cells using the average concentrations shown in Figure 3 (omitting the value of N, since this was under the detection limit of our instruments), one can confirm the higher resistance against corrosion of the cell's borders (PREN ≈ 27.4) compared to the cell's interior (PREN ≈ 24.8). From Figure 7 it can be seen that the borders of the cells represent a physical barrier for the corrosion attack. This could be the reason why in the AM samples the corrosion is rather superficial when compared to the attack on the wrought material. Figure 8 presents examples of depth profiles acquired on corrosion spots on the wrought and the LMD 316L samples. Variations in the corrosion depth were seen within one sample depending on the corrosion spot analyzed. However, in general, the trend in corrosion depth is similar to that shown in Figure 8. Much deeper and wider pits were found on the wrought 316L stainless steel sample compared to those seen on the surface of the AM 316L specimens, where the sizes were limited by the dimensions of the cells.

3.4. SKPFM analysis

Figure 9 portrays the topography and corresponding Volta potential map of an area in the polished surface of the LMD 316L stainless steel sample obtained by SKPFM. The topography

shows a relatively flat substrate with a nanoscale roughness of R_a = 6.5 nm (Figure 9a). The features observed in the potential map (Figure 9b) are independent from those seen in the topography. While no microstructural characteristic can be recognized in the topography image, the typical cells described in previous sections (Figure 2) are clearly visible on the Volta potential map. This undoubtedly indicates that no topographical effect has influenced the Volta potential values measured. The borders of these cells can be easily recognized, having a relatively higher Volta potential value than the inner part of the cells. This higher nobility at the borders can be due to the local enrichment of alloying elements (such as Cr, Ni, Mo, Mn, and Si) and depletion of Fe in these regions. Figure 9c shows the potential profile of the line represented in the inset of Figure 9b. As can be seen, the potential of the border of the cells is on average 10 mV higher than that of the cells' interior. The same SKPFM mapping was carried out for the SLM specimen. However, no clear feature could be distinguished in the Volta potential map. Andreatta et al. [16] was also unable to recognize any microstructural feature in the Volta potential map of an SLM 316L stainless steel. This could be due to the fact that the microstructure of the SLM sample is much finer than that of the LMD material (see Figure 2), and the potential differences are within the noise level of the equipment. Kong et al [34] reported a Volta potential difference of only 5 mV between the border and the interior of the cells in an SLM 316L stainless steel sample, while Andreatta et al. [16] reported a 4mV difference between the maximum and the minimum voltage measured in a line scan also for SLM 316L stainless steel. The slightly higher nobility of the borders of the cells compared to their inner part is in perfect agreement with the higher corrosion and etch resistance of these borders.

4. Discussion

The inherent characteristics of the additive manufacturing processes used to fabricate the samples analyzed in this work (LMD and SLM), have clearly a considerable impact on the microstructure and consequently on the corrosion resistance of these materials. The cells present on the microstructure of the LMD 316L specimen were on average much larger than those found on the SLM samples. This could be due to the differences in the laser characteristics (laser power and spot size), which can greatly affect the energy density input and the cooling rate/gradient. These parameters have already been shown to greatly influence the size of the microstructure in AM 316L stainless steel [24]. In general, the mode of solidification and the refinement of the features are determined by the thermal gradient (G) and the growth rate (R) [38]. The multiplication of these two magnitudes (G×R) determines the cooling rate and how fine the structure would be: the higher this product, the finer the structure. The larger laser spot diameter and layer thickness of the LMD process compared to the SLM method could lead to a relatively lower thermal gradient/cooling rate, which can explain the larger cellular structure found in the LMD samples in comparison with the SLM specimens.

Previous studies have shown that the thickness and chemical composition of the native oxide of AM 316L stainless steel is comparable to that of wrought material [16-18,35]. Nevertheless, in a recent work we demonstrated that despite the similarities in thickness and chemical composition,

significant differences exist in the dielectric properties and conductivity profile of the passive oxide layers of SLM and wrought 316L stainless steel, suggesting the existence of structural differences between them [35]. The passive film in SLM 316L specimens has shown better barrier properties and higher stability than that of wrought specimens [17,18,34,35]. The unique segregation of alloying elements in AM 316L stainless steel, forming an interconnected and 3-dimensional network, seems to be the cause for the high stability of the native oxide under the presence of corrosive media. Previous studies suggest that this elemental segregation, and therefore the compositional gradient created, could be the cause for the relatively high concentration of dislocations found at the cell's borders [39]. Dislocations are generally regarded as high energy sites, presenting a relatively higher chemical potential than the surrounding matrix. Kong et al. [34] and Man et al. [33] suggested that the borders of the cells present in the microstructure of SLM 316L stainless steel increases the number of nucleation sites for passive film formation, promoting the growth of a more continuous and stable passive film. The higher density of cells borders (number of borders per surface area) present on the SLM sample compared to the LMD specimen, could, therefore, represent a higher density of nucleation sites for the formation of a continuous, stable, and less defective native oxide film. Moreover, previous studies have shown that Mo on stainless steel can modify the passive oxide layer, making it more stable under the presence of Cl^- ions [40]. Consequently, the finer Mo-rich network of the SLM material compared to that of the LMD sample could render the passive film of the SLM specimen more stable against breakdown caused by the attack of aggressive ions in a corrosive medium. This could explain the extended passivity of the SLM sample compared to the LMD material, and also the larger passivity shown by the AM specimens compared to the wrought sample. Therefore, a direction to be explored by AM 316L stainless steel manufacturers in order to produce highly corrosion-resistant parts could focus on the adjustment of process parameters to develop materials with the finest possible cellular structure, while keeping it also free of pores.

Moreover, the very high corrosion resistance shown by the borders of the cells together with the fact that these borders form an interconnected 3-dimensional network, make these networks to be an inherent barrier that limits the further propagation of corrosion into the material. This was clearly seen in the differences in the measured amount of charge during anodic dissolution (see Figure 5) between the wrought material (with no protective internal network) and the AM specimens (with a protective (Cr,Ni,Mo,Mn,Si)–rich network). Much more material was removed after passivity breakdown during anodic polarization for the wrought sample than for the AM specimens. Interestingly, even though great differences were seen in the size of the cells constituting the network, approximately the same amount of charge due to the anodic dissolution of the steel matrix was measured for the LMD and SLM 316L samples. This suggests that the sole existence of this network within the 316L stainless steel matrix represents a physical barrier that contains the corrosion attack from further propagating into the material. Moreover, the extent of this containment seems to be independent of the dimensions of the cells forming the network.

In general, considering this and our previous study [35], we believe that a major factor influencing the passivity of these materials is the stability and barrier properties of the native oxide layer. Nevertheless, further studies on the effect of porosity, the formation of inclusions, grain size, and residual stresses should be considered in future works to better understand the influence of the additive manufacturing process on the corrosion behavior of these materials. Differences in process parameters during MAM can lead to variations in cooling rates and thermal gradients during the printing process, which could, as a result, lead to differences in residual stresses and grain size in the AM specimens. Residual stresses and grain size can, in general, influence the surface energy and therefore, the nucleation and growth of the native oxide film. This can affect the barrier properties of this oxide, and hence the passivity of the material. Some researchers claim that the existence of compressive residual stresses in 316L stainless steel prepared by SLM could be the cause for the higher corrosion resistance of as-built specimens compared to materials that underwent stress relief heat treatments [41]. Nevertheless, we believe that the link between residual stresses and corrosion resistance is not a straight forward relationship. Residual stresses can also affect the materials susceptibility to stress corrosion cracking.

5. Conclusions

The corrosion behavior of 316L stainless steel specimens prepared using two different additive manufacturing methods (SLM and LMD) was assessed and compared with each other and with that of a wrought sample. The main conclusions of this work can be summarized as follows:

1. The microstructure of additively manufactured 316L stainless steel consists of a 3-dimensional network of cells, with borders slightly enriched in Cr, Ni, Mo, Si, and Mn, and depleted in Fe.
2. As seen in the surface morphology after the corrosion attack, the borders of the cells present in the microstructure of AM 316L stainless steel are highly resistant against corrosion. Due to the high corrosion resistance of these cell's borders, the corrosion attack is partly contained from further propagating into the material, limiting the amount of material removed during corrosion.
3. The size of the cells found in the microstructure of AM 316L stainless steel is greatly affected by the conditions of the additive manufacturing process. The cells present on the specimens prepared by LMD were about 10 times larger than those found in SLM samples.
4. LMD, SLM, and wrought 316L stainless steel presented very similar corrosion potential and passive current density values. Nevertheless, a much wider passivity was found in the SLM specimen (~1155 mV), followed by the LMD sample (~571 mV), and finally by the wrought material (~499 mV), which presented the lowest corrosion resistance.
5. The differences in the passivity of the LMD and SLM 316L specimens seem to be associated with the marked differences seen in the dimensions of the microstructural features of these two samples. The much finer microstructure (distribution of alloying

elements) of SLM specimens compared to LMD samples could lead to the growth of a more compact, stable, and less defective native oxide.

Data availability

The raw/processed data required to reproduce these findings cannot be shared at this time as the data also forms part of an ongoing study.

Acknowledgements

This research was supported by the FWO (Flemish Science Foundation) under research project S009319N (Hi-PAS-project). Bart Lippens from the department MACH of the Vrije Universiteit Brussel is also acknowledged for his contribution with the samples polishing.

References

1. S. Gorsse, C. Hutchinson, M. Goune, R. Banerjee, Additive manufacturing of metals: a brief review of the characteristic microstructures and properties of steels, Ti-6Al-4V and high-entropy alloys, Sci. Technol. Adv. Mater. 18 (2017) 584-610.
2. D.D. Gu, W. Meiners, K. Wissenbach, R. Poprawe, Laser additive manufacturing of metallic components: materials, processes and mechanisms, Int. Mater. Rev. 57 (2012) 133-164.
3. L.E. Murr, S.M. Gaytan, D.A. Ramirez, E. Martinez, J. Hernandez, K.N. Amato, P.W. Shindo, F.R. Medina, R.B. Wicker, Metal fabrication by additive manufacturing using laser and electron beam melting technologies, J. Mater. Sci. Technol. 28 (2012) 1-14.
4. L.E. Murr, E. Martinez, K.N. Amato, S.M. Gaytan, J. Hernandez, D.A. Ramirez, P.W. Shindo, F. Medina, R.B. Wicker, Fabrication of metal and alloy components by additive manufacturing: examples of 3D materials science, J. Mater. Res. Technol. 1 (2012) 42-54.
5. D. Herzog, V. Seyda, E. Wycisk, C. Emmelmann, Additive manufacturing of metals, Acta Mater. 117 (2016) 371-392.
6. W.J. Sames, F.A. List, S. Pannala, R.R. Dehoff, S.S. Babu, The metallurgy and processing science of metal additive manufacturing, Int. Mater. Rev. 61 (2016) 315-360.
7. ISO / ASTM52900-15, Standard Terminology for Additive Manufacturing – General Principles – Terminology, ASTM International, West Conshohocken, PA, 2015.
8. G.F. Sun, X.T. Shen, Z.D. Wang, M.J. Zhan, S. Yao, R. Zhou, Z.H. Ni, Laser metal deposition as repair technology for 316L stainless steel: Influence of feeding powder compositions on microstructure and mechanical properties, Opt. Laser Technol. 109 (2019) 71-83.
9. K. Saeidi, X. Gao, F. Lofaj, L. Kvetkova, Z.J. Shen, Transformation of austenite to duplex austenite-ferrite assembly in annealed stainless steel 316L consolidated by laser melting, J. Alloys Compd. 633 (2015) 463-468.
10. K. Saeidi, X. Gao, Y. Zhong, Z.J. Shen, Hardened austenite steel with columnar sub-grain structure formed by laser melting, Mater. Sci. Eng. A 625 (2015) 221-229.

11. T. Kurzynowski, K. Gruber, W. Stopyra, B. Kuznicka, E. Chlebus, Correlation between process parameters, microstructure and properties of 316L stainless steel processed by selective laser melting, Mater. Sci. Eng. A 718 (2018) 64-73.
12. Y. Zhong, L. Liu, S. Wikman, D. Cui, Z. Shen, Intragranular cellular segregation network structure strengthening 316L stainless steel prepared by selective laser melting, J. Nucl. Mater. 470 (2016) 170-178.
13. M. Godec, S. Zaefferer, B. Podgornik, M. Šinko, E. Tchernychova, Quantitative multiscale correlative microstructure analysis of additive manufacturing of stainless steel 316L processed by selective laser melting, Mater. Charact. 160 (2020) 110074.
14. E. Liverani, S. Toschi, L. Ceschini, A. Fortunato, Effect of selective laser melting (SLM) process parameters on microstructure and mechanical properties of 316L austenitic stainless steel, J. Mater. Process. Technol. 249 (2017) 255–263.
15. J.A. Cherry, H.M. Davies, S. Mehmood, N.P. Lavery, S.G.R. Brown, J. Sienz, Investigation into the effect of process parameters on microstructural and physical properties of 316L stainless steel parts by selective laser melting, Int. J. Adv. Manuf. Technol. 76 (2015) 869–879.
16. F. Andreatta, A. Lanzutti, E. Vaglio, G. Totis, M. Sortino, L. Fedrizzi, Corrosion behaviour of 316L stainless steel manufactured by selective laser melting, Mater. Corr. (2019) 1-13.
17. M.J.K. Lodhi, K.M. Deen, M.C. Greenlee-Wacker, W. Haider, Additively manufactured 316L stainless steel with improved corrosion resistance and biological response for biomedical applications, Addit. Manuf. 27 (2019) 8-19.
18. M.J.K. Lodhi, K.M. Deen, W. Haider, Corrosion behavior of additively manufactured 316L stainless steel in acidic media, Materialia 2 (2018) 111-121.
19. J.R. Trelewicz, G.P. Halada, O.K. Donaldson, G. Manogharan, Microstructure and corrosion resistance of laser additively manufactured 316L stainless steel, J. Mater. 68 (2016) 850-859.
20. M. Zietala, T. Durejko, M. Polanski, I. Kunce, T. Plocinski, W. Zielinski, M. Lazinska, W.Stepniowski, T. Czujko, K.J. Kurzydlowski, Z. Bojar, The microstructure, mechanical properties and corrosion resistance of 316L stainless steel fabricated using laser engineered net shaping, Mater. Sci. Eng. A 677 (2016) 1-10.
21. B. Barkia, P. Aubry, P. Haghi-Ashtiani, T. Auger, L. Gosmain, F. Schuster, H. Maskrot, On the origin of the high tensile strength and ductility of additively manufactured 316L stainless steel: Multiscale investigation, J. Mater. Sci. Technol. 41 (2020) 209–218.
22. A. Saboori, A. Aversa, F. Bosio, E. Bassini, E. Librera, M. De Chirico, S. Biamino, D. Ugues, P. Fino, M. Lombardi, An investigation on the effect of powder recycling on the microstructure and mechanical properties of AISI 316L produced by Directed Energy Deposition, Mater. Sci. Eng. A 766 (2019) 138360.

23. Z.E. Tan, J.H.L. Pang, J. Kaminski, H. Pepin, Characterisation of porosity, density, and microstructure of directed energy deposited stainless steel AISI 316L, Addit. Manuf. 25 (2019) 286–296.
24. M.H. Farshidianfar, A. Khajepour, A.P. Gerlich, Effect of real-time cooling rate on microstructure in Laser Additive Manufacturing, J. Mater. Process. Technol. 231 (2016) 468–478.
25. Y. Sun, A. Moroz, K. Alrbaey, Sliding wear characteristics and corrosion behaviour of selective laser melted 316L stainless steel, J. Mater. Eng. Perform. 23 (2014) 518-526.
26. D. Kong, X. Ni, C. Dong, L. Zhang, C. Man, J. Yao, K. Xiao, X. Li, Heat treatment effect on the microstructure and corrosion behavior of 316L stainless steel fabricated by selective laser melting for proton exchange membrane fuel cells, Electrochimica Acta 276 (2018) 293-303.
27. M. Laleh, A.E. Hughes, W. Xua, N. Haghdadi, K. Wang, P. Cizek, I. Gibson, M.Y. Tan, On the unusual intergranular corrosion resistance of 316L stainless steel additively manufactured by selective laser melting, Corr. Sci. 161 (2019) 108189.
28. X. Ni, D. Kong, W. Wu, L. Zhang, C. Dong, B. He, L. Lu, K. Wu, D. Zhu, Corrosion Behavior of 316L Stainless Steel Fabricated by Selective Laser Melting Under Different Scanning Speeds, J. Mater. Eng. Perform. 27 (2018) 3667-3677.
29. Y. Zhang, J. Zhang, Q. Yan, L. Zhang, M. Wang, B. Song, Y. Shi, Amorphous alloy strengthened stainless steel manufactured by selective laser melting: Enhanced strength and improved corrosion resistance, Scripta Materialia 148 (2018) 20-23.
30. Q. Chao, V. Cruz, S. Thomas, N. Birbilis, P. Collins, A. Taylor, P.D. Hodgson, D. Fabijanic, On the enhanced corrosion resistance of a selective laser melted austenitic stainless steel, Scripta Materialia 141 (2017) 94-98.
31. S.H. Sun, T. Ishimoto, K. Hagihara, Y. Tsutsumi, T. Hanawa, T. Nakano, Excellent mechanical and corrosion properties of austenitic stainless steel with a unique crystallographic lamellar microstructure via selective laser melting, Scripta Materialia 159 (2019) 89–93.
32. G. Sander, S. Thomas, V. Cruz, M. Jurg, N. Birbilis, X. Gao, M. Brameld, C.R. Hutchinson, On the corrosion and metastable pitting characteristics of 316L stainless steel produced by selective laser melting, J. Electrochem. Soc. 164 (2017) C250-C257.
33. C. Man, C. Dong, T. Liu, D. Kong, D. Wang, X. Li, The enhancement of microstructure on the passive and pitting behaviors of selective laser melting 316L SS in simulated body fluid, Appl. Surf. Sci. 467–468 (2019) 193–205.
34. D. Kong, C. Dong, X. Ni, L. Zhang, H. Luo, R. Li, L. Wang, C. Man, X. Li, The passivity of selective laser melted 316L stainless steel, Appl. Surf. Sci. 504 (2020) 144495.
35. R.I. Revilla, B. Wouters, F. Andreatta, A. Lanzutti, L. Fedrizzi, I. De Graeve, EIS comparative study and critical Equivalent Electrical Circuit (EEC) analysis of the native

oxide layer of additive manufactured and wrought 316L stainless steel, Corr. Sci. 167 (2020) 108480.
36. P. Ganesh, R. Giri, R. Kaul, P.R. Sankar, P. Tiwari, A. Atulkar, R.K. Porwal, R.K. Dayal, L.M. Kukreja, Studies on pitting corrosion and sensitization in laser rapid manufactured specimens of type 316L stainless steel, Mater. Design 39 (2012) 509-521.
37. J. Dutta Majumdar, A. Pinkerton, Z. Liu, I. Manna, L. Li, Mechanical and electrochemical properties of multiple-layer diode laser cladding of 316L stainless steel. Appl. Surf. Sci. 247 (2005) 373-377.
38. M.E. Glicksman, Principles of solidification. New York: Springer; 2011.
39. D. Kong, X. Ni, C. Dong, X. Lei, L. Zhang, C. Man, J. Yao, X. Cheng, X. Li. Bio-functional and anti-corrosive 3D printing 316L stainless steel fabricated by selective laser melting. Mater. Des. 152 (2018) 88-101.
40. A. Pardo, M.C. Merino, A.E. Coy, F. Viejo, R. Arrabal, E. Matykina, Pitting corrosion behaviour of austenitic stainless steels – combining effects of Mn and Mo additions, Corr. Sci. 50 (2008) 1796-1806.
41. D. Kong, C. Dong, X. Ni, L. Zhang, J. Yao, C. Man, X. Cheng, K. Xiao, X. Li. Mechanical properties and corrosion behavior of selective laser melted 316L stainless steel after different heat treatment processes. J. Mater. Sci. Technol. 35 (2019) 1499-1507.

Figures

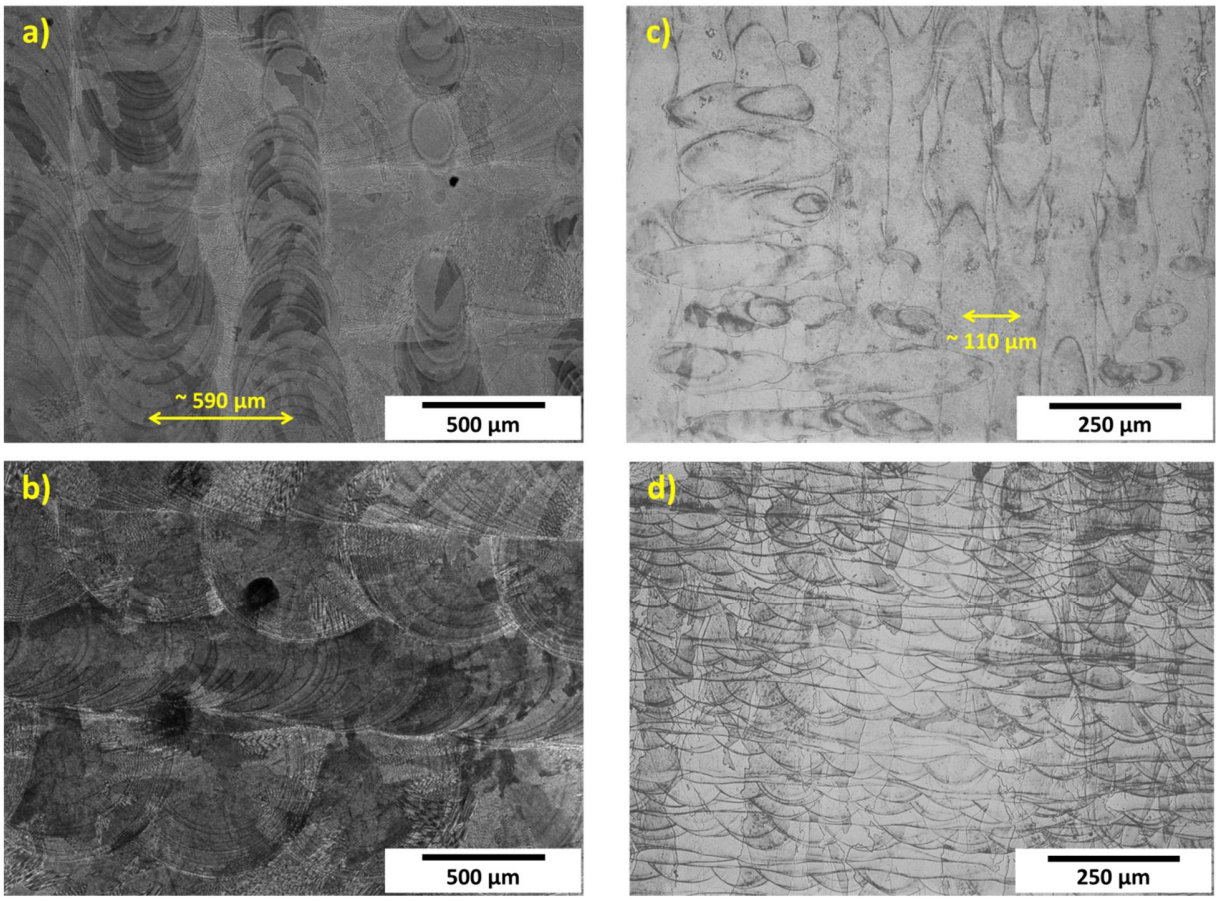

Figure 1. Optical images of the etched surface of the LMD (a,b) and SLM (c,d) 316L stainless steel.

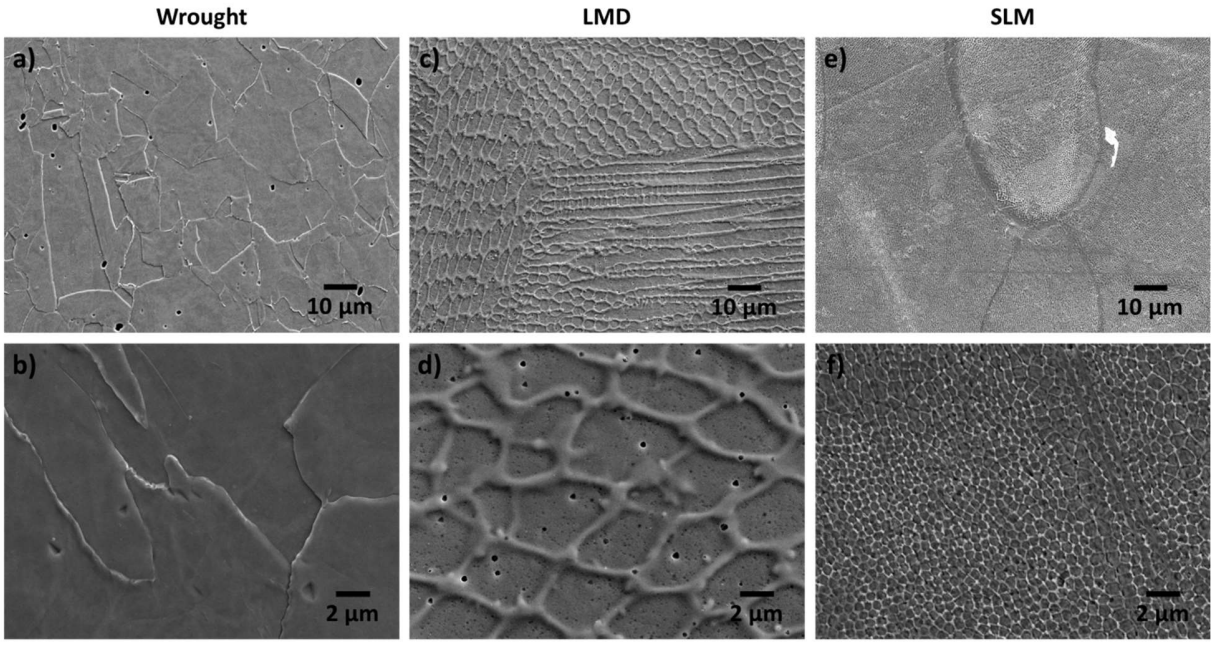

Figure 2. Secondary electron images of the etched surface of the wrought (a,b) and additive manufactured 316L stainless steel prepared using LMD (c,d) and SLM (e,f). Top micrographs were taken at middle magnification while bottom micrographs were acquired at higher magnification.

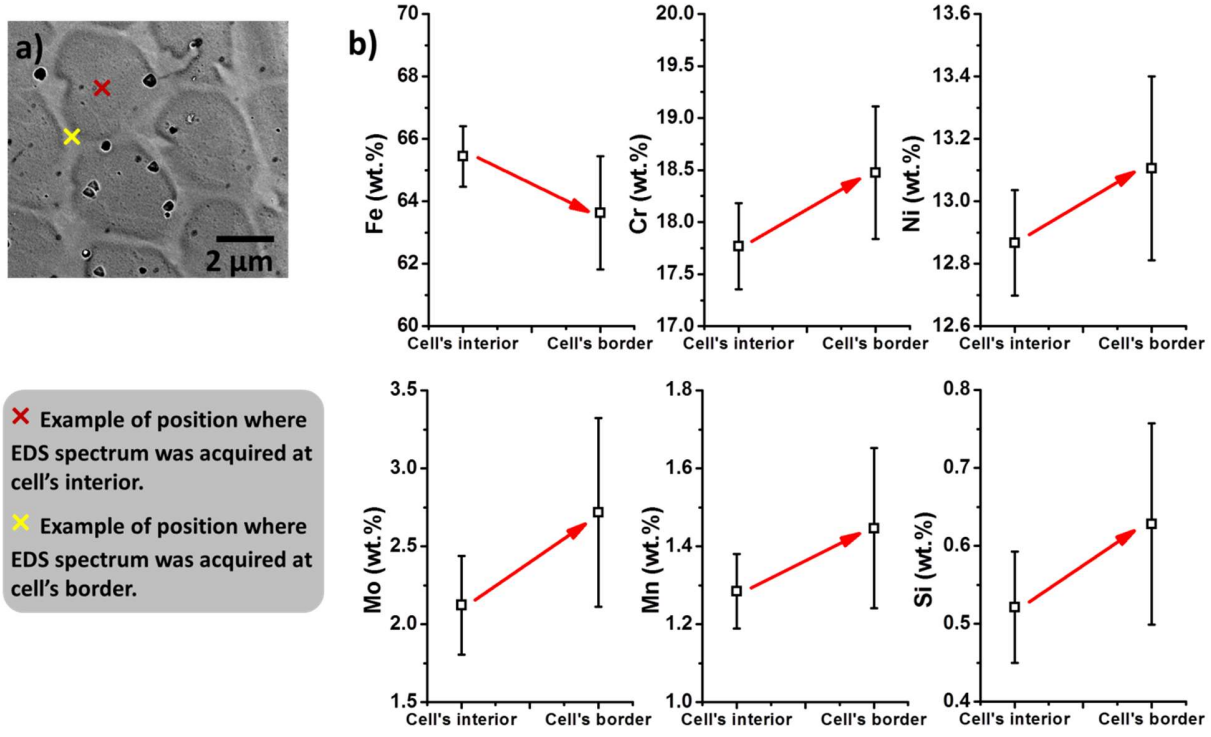

Figure 3. EDS analysis conducted to estimate the chemical composition at the cells' border and at the cells' interior. (a) Schematic showing examples of positions where the EDS spectra were acquired. (b) Results of the EDS compositional analysis.

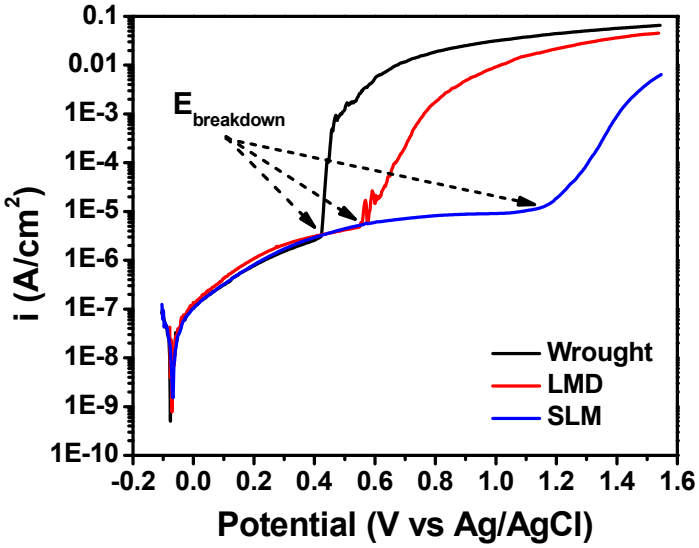

Figure 4. Potentiodynamic polarization curves of wrought, LMD, and SLM 316L stainless steel specimens in 3.5 wt.% NaCl.

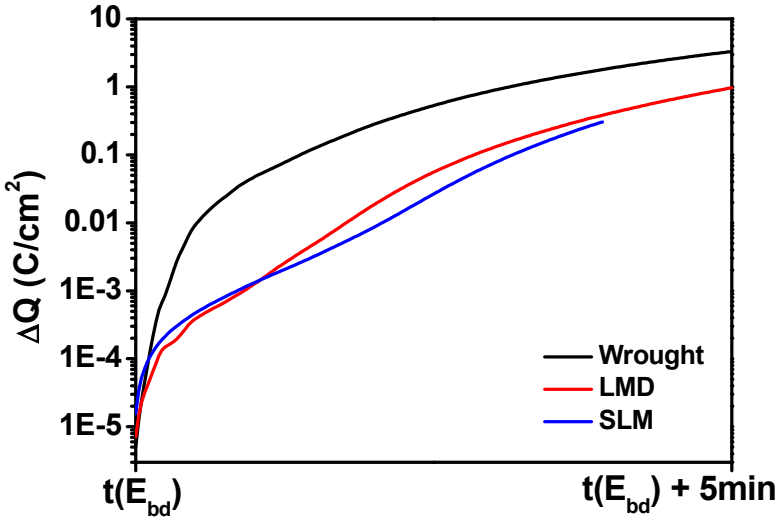

Figure 5. Amount of charge per surface area calculated for the wrought, LMD, and SLM 316L stainless steel from the moment of passivity breakdown based on their potentiodynamic polarization curves. E_{bd} refers here to the breakdown potential ($E_{breakdown}$).

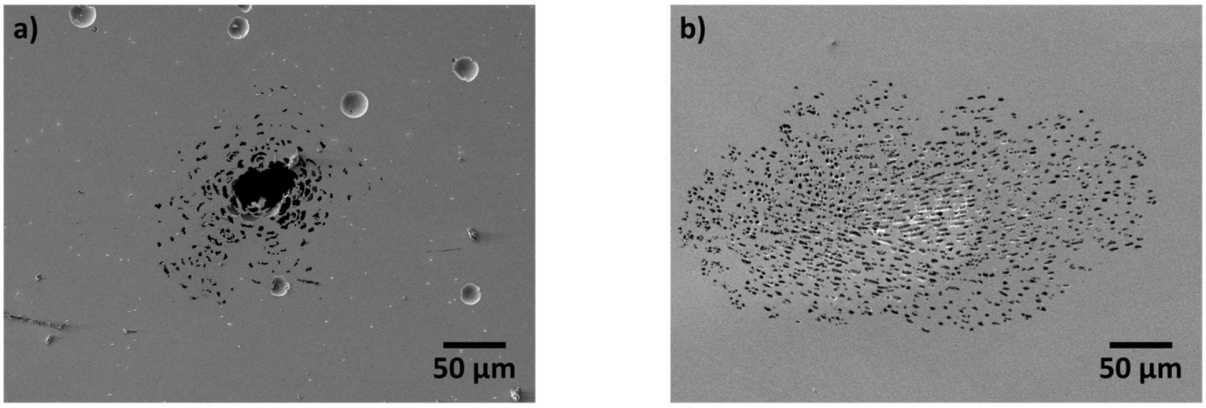

Figure 6. Secondary electron images of the corrosion attack after the potentiodynamic polarization experiments for the wrought (a) and LMD (b) 316L stainless steel.

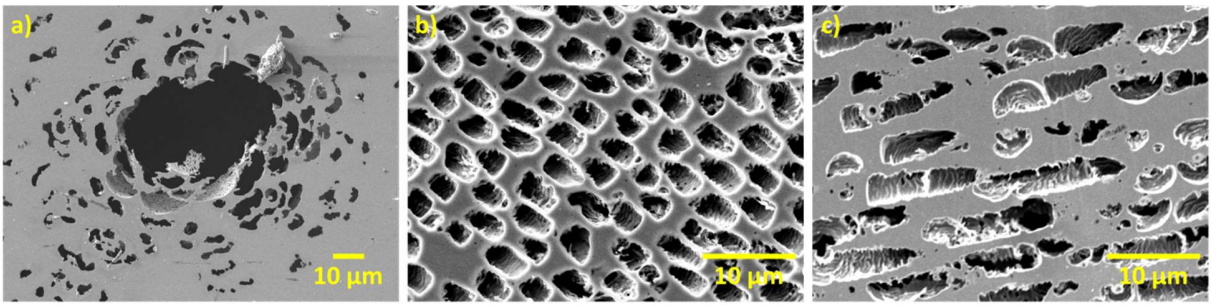

Figure 7. High magnification secondary electron images of the corrosion attack after the potentiodynamic polarization experiments for the wrought (a) and LMD (b,c) 316L stainless steel. (b) and (c) show different corroded spots of the same surface (one in which the rounder side of the cells is seen and the other in which the elongated section is displayed).

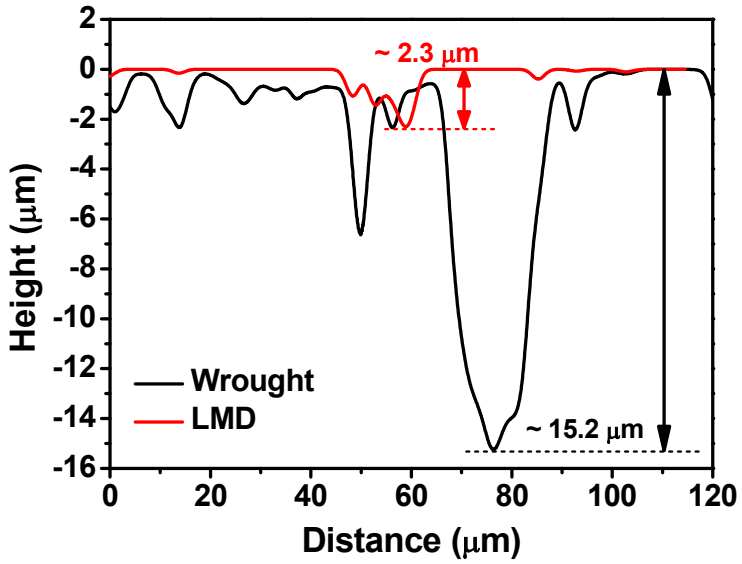

Figure 8. Examples of depth profiles of corrosion spots in the wrought and LMD 316L stainless steel obtained using a Leica DMi8 optical microscope.

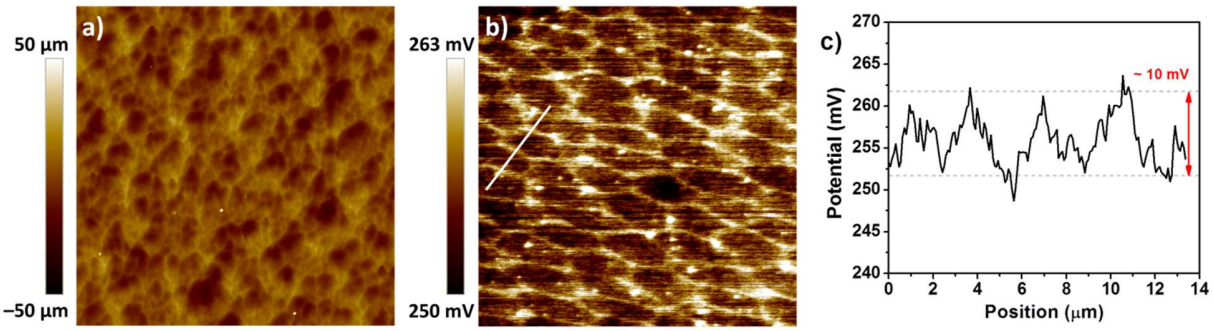

Figure 9. (a) Topography and (b) potential map of an area in the surface of the LMD 316L stainless steel sample. Scan size: 40 µm × 40 µm. (c) Potential profile of the line represented in (b).

Tables

Table 1. Nominal chemical composition (wt.%) of 316L stainless steel.

Cr	Ni	Mo	Mn	Si	S	C	N	P	Fe
16 – 18	10 – 14	2 – 3	< 2	< 0.75	< 0.03	< 0.03	< 0.1	< 0.045	Balance

Table 2. Passivity region calculated as the difference between $E_{breakdown}$ and E_{corr} from the potentiodynamic polarization experiments for the wrought, LMD, and SLM 316L stainless steel.

	$E_{breakdown} - E_{corr}$ (mV)
Wrought	499 ± 2
LMD	571 ± 26
SLM	1155 ± 66